

Oriented silver oxide nanostructures synthesized through a template-free electrochemical route

Weifeng Wei, Xuhui Mao, Luis A. Ortiz and Donald R. Sadoway*

Received 9th July 2010, Accepted 27th September 2010

DOI: 10.1039/c0jm02214d

Oriented silver oxide nanostructures, including polycrystalline columnar structures, nanofibers and single crystalline nanodisks, were successfully grown on conductive substrates from acetate-containing aqueous solutions through an electrochemical strategy. The morphological features (shape, diameter and areal density) of the Ag_xO nanostructures could be effectively adjusted through deposition parameters, including current density, concentration of silver nitrate and solution pH values. Structural and chemical analyses, based on HRTEM/SAED and XPS techniques, confirm that the electrodeposited Ag_xO nanostructures have a defective cubic Ag_2O structure containing cation deficiency, twin boundaries, and amorphous zones and stacking faults. The variety of nanostructures obtained in this work can be attributed to the kinetic effect of supersaturation ratio of Ag_xO at the electrode/electrolyte interface. This electrochemical process is versatile to extend to other transition metal oxides and to a variety of inexpensive conductive substrates.

1. Introduction

Metal oxides in the Ag–O system, including Ag_2O , AgO , Ag_3O_4 and Ag_2O_3 , constitute a fascinating group of inorganic materials.¹ Silver oxides crystallize in various types of crystal structures, leading to a variety of interesting physicochemical properties such as catalytic, electrochemical, electronic and optical properties. Therefore, silver oxide nanocrystals and thin films have been intensively pursued for promising applications as a catalyst for ethylene and methanol oxidation,^{2,3} as a sensor for the detection of carbon monoxide and ammonia,^{4–7} as photovoltaic materials,^{8–10} as important components in optical memories¹¹ and plasmon photonic devices,¹² or as active cathode materials in silver oxide/zinc alkaline batteries.^{13,14} The properties of silver oxide nanostructures and thin films are found to be vitally sensitive to the growth method and the experimental conditions applied.

Inspired by these considerations, a variety of techniques has been employed to grow silver oxide nanostructures and thin films with desirable morphologies, crystal structures, cation distributions and oxidation states. Reactive sputtering of silver metal in an oxygen-containing argon atmosphere^{1,11,15–24} and thermal/electron-beam evaporation of silver metal followed by oxidation^{25,26} are two extensively used techniques. High growth temperatures of these gas-phase synthesis techniques, however, limit the types of substrate materials and the scope of phase structures in which silver oxide nanostructures can be deposited. It would therefore be of great interest to develop alternative techniques to synthesize electrode materials at lower temperatures. In such regard, wet-chemistry (hydrothermal or solvothermal) and electrochemical methods are the most appealing ways to form nanostructured oxides.^{27,28} Wet-chemistry methods generally require the substrates to be dipped inside

the precursor solution for days to form nanostructured materials at temperatures ranging from 120 to 200 °C. Electrochemical deposition offers a more time-efficient way (<2 h) to grow nanostructured materials at even lower temperatures (<90 °C), making it one of the best low-temperature methods available for growth of nanostructured materials on conductive substrates.²⁹

Silver oxides have been prepared electrochemically as continuous films,^{9,10} as particles or nanoparticles using a sacrificial Ag wire anode,⁵ or as microwires by electrochemical step edge decoration (ESED) on conductive substrates.^{6,7} However, there are no reports in the open literature of direct growth of silver oxide nanostructures with well-defined morphologies on conductive substrates from aqueous solutions. The electrochemical mechanism underlying such a controlled-growth process is still unclear. In the present study, oriented silver oxide nanostructures were electrochemically deposited on conductive substrates without using sacrificial templates. The physical features, including the shape, size and crystal structure, of the oriented silver oxide nanostructures were manipulated by varying solution composition, solution pH value and applied overpotential (current density). The correlation between deposition parameters (supersaturation ratio) and physical features of Ag_xO nanostructures was illustrated.

2. Experimental

2.1. Materials synthesis

Silver oxide nanostructures were anodically electrodeposited on Au-coated (100 nm thick) glass substrates from 0.1 M sodium acetate solutions with various AgNO_3 concentrations under galvanostatic control with current densities ranging from 0.1 to 50 mA cm^{-2} . Before electrodeposition, the Au-coated glass substrates were ultrasonically cleaned in acetone and ethanol for 10 min, respectively. Electrochemical deposition was performed with a Solartron 1286A potentiostat/galvanostat, and a three-electrode cell configuration. The Au-coated glass served as the

Department of Materials Science and Engineering, Massachusetts Institute of Technology, Cambridge, MA, 02139, USA. E-mail: dsadoway@mit.edu; Fax: +1-617-253-5418; Tel: +1-617-253-3487

working electrode with a platinum mesh counter electrode and an Ag/Ag⁺ reference electrode. The working electrode and counter electrode were placed in vertical opposition of one another with an inter-electrode gap of 20 mm. The electrolyte pH values were varied using dilute HNO₃ and NaOH solutions. After electrodeposition, the working electrodes were rinsed with deionized water, dried at room temperature in air and then stored in a vacuum desiccator.

2.2. Materials characterization

The morphology and chemistry of the as-prepared silver oxide electrodes were analyzed in a JEOL 6320FV field emission scanning electron microscope (FE-SEM). Chemical state analysis was carried out by X-ray photoelectron spectroscopy (XPS) using a Kratos AXIS Ultra X-ray photoelectron spectrometer. A monochromatic Al source, operating at 150 W with a pass energy of 160 eV and a step size of 0.5 eV, was utilized to collect survey spectra. As for high resolution spectra, a pass energy of 20 eV and a step size of 0.1 eV were employed. All XPS spectra were corrected using the C 1s line at 284.6 eV. Curve fitting, background subtraction and quantitative information evaluation were accomplished by using Casa XPS Version 2.3.13 software. The crystal structure and morphology of the deposited silver oxide nanostructures were investigated using a JEOL 2010 transmission electron microscope (TEM) equipped with an Oxford ultra-thin window (UTW) X-ray detector. Electron transparent samples were prepared by scraping off the silver oxide deposits and ultrasonic dispersion in methanol for 10 min. One or two drops of the suspension were cast on 300 mesh, carbon-coated Cu grids and allowed to dry in air.

3. Results and discussion

3.1. Surface morphology

The synthesis of silver oxide nanostructures involved the deposition of Ag_xO generated from aqueous Ag(I) acetate solutions on Au-coated glass electrode surfaces. Fig. 1 shows the morphology of Ag_xO deposited from a 0.001 M AgNO₃–0.1 M sodium acetate solution at its natural pH of 7.80 under various current densities. No Ag_xO deposits could be observed at current densities lower than 1 mA cm⁻². Upon increasing the current density from 1 mA cm⁻² to 50 mA cm⁻², the Ag_xO morphology evolves from sparse oxide plates (Fig. 1a) to columnar features (Fig. 1b–d), while the diameter of Ag_xO columns appears to increase from hundreds of nanometres to several microns with elevating current density. From the high resolution SEM images (insets in Fig. 1a–c), it can be seen that the Ag_xO deposits are generally composed of stacked oxide nanoparticles with diameters ranging from 10 nm to 50 nm.

Varying the solution pH values could also make a significant influence on the morphology of Ag_xO deposits. When deposited at pH = 2.0, the Ag_xO columns have diameters of 300 nm to 500 nm with a very sparse distribution (Fig. 2a). The Ag_xO columns become much finer (diameters of 100 nm to 200 nm) and denser when the solution pH value is raised to 4.0 (Fig. 2b). Increasing the solution pH to 9.5 results in coarser Ag_xO columns that have a lower areal density and many scattered

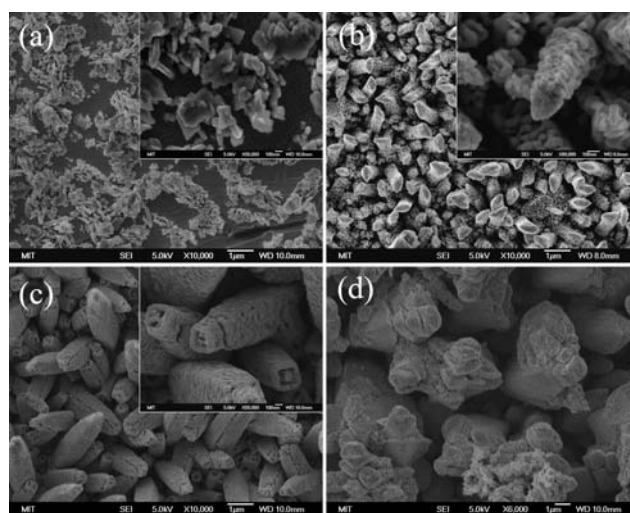


Fig. 1 SEM morphology of Ag_xO electrodes prepared under different current densities from 0.001 M AgNO₃ + 0.1 M Na acetate solutions at a pH value of 7.8: (a) 1 mA cm⁻², (b) 5 mA cm⁻², (c) 20 mA cm⁻² and (d) 50 mA cm⁻².

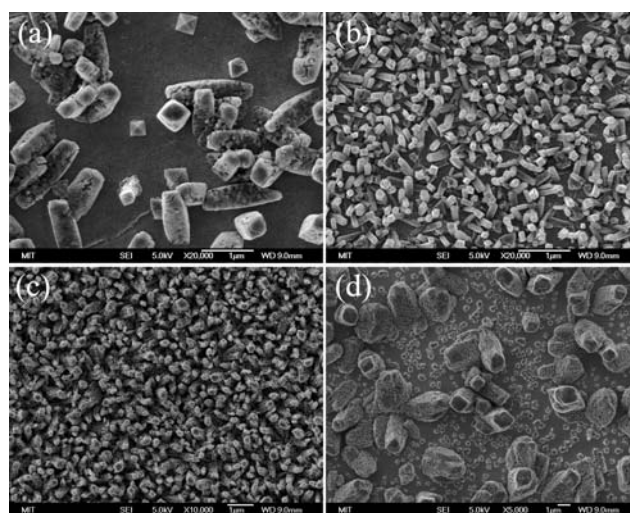


Fig. 2 SEM morphology of Ag_xO electrodes prepared from 0.001 M AgNO₃–0.1 M Na acetate solutions with various pH values: (a) pH = 2.0, (b) pH = 4.0, (c) pH = 6.0 and (d) pH = 9.5. The deposition current density is 5 mA cm⁻².

oxide particles among the columns. Near neutral pH values are favorable to achieve fine Ag_xO columns with high areal density.

At an electrolyte concentration of 0.05 M AgNO₃ (with 0.1 M sodium acetate), the relationship between current density and morphology changes in electrodeposition products of Ag_xO is much different than at lower concentrations. At a current density of 5 mA cm⁻², micro-scale oxide particles plus nanoscale fibers are apparent in the Ag_xO deposit (Fig. 3a). It is interesting to note that there are numerous pinholes in the micro-scale oxide particles (inset of Fig. 3a). As the current densities were reduced down to 1 and 0.1 mA cm⁻², nanofibers with an average diameter of ~30 nm (Fig. 3b) and interconnected nanodisks with 300–500 nm in diameter and ~50 nm thickness (Fig. 3c and d), were deposited.

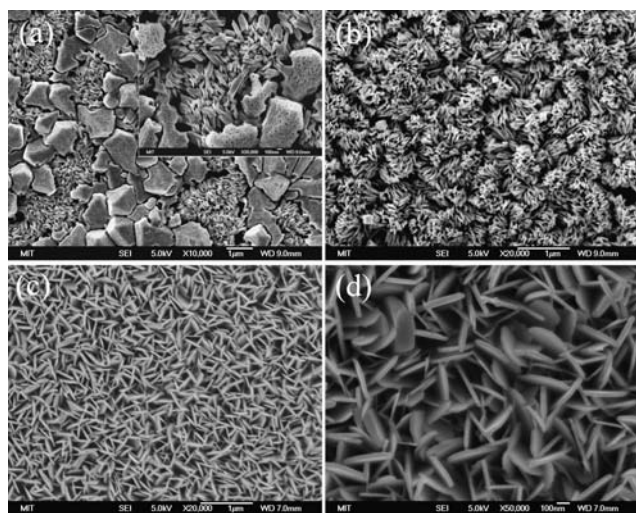


Fig. 3 SEM morphology of Ag_xO electrodes prepared from a 0.05 M AgNO_3 -0.1 M Na acetate solution at a pH value of 7.0: (a) $i = 5 \text{ mA cm}^{-2}$; (b) $i = 1 \text{ mA cm}^{-2}$; (c and d) $i = 0.1 \text{ mA cm}^{-2}$.

3.2. Deposit chemistry

XPS was employed to analyze the chemical state of the as-deposited Ag_xO nanostructures. It was found that similar XPS spectra could be obtained from the as-deposited Ag_xO nanostructures prepared under various deposition conditions. Fig. 4 shows a representative survey spectrum and high-resolution Ag 3d and O 1s spectra taken from the Ag_xO deposits. The Ag to O ratio in the Ag_xO deposits was estimated to be close to 1 : 1 based on the survey spectrum, taking the absorbed hydrated species into account (Fig. 4a). The peak shape of the Ag $3d_{5/2}$ and Ag $3d_{3/2}$ levels (Fig. 4b) suggests that a single Gaussian-Lorentzian peak function cannot be applied to fit each Ag 3d level

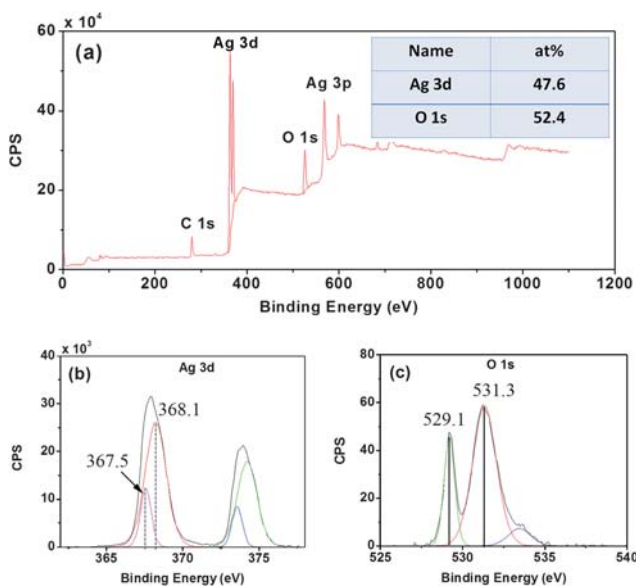


Fig. 4 Representative XPS spectra taken from the as-deposited Ag nanostructures. (a) Survey spectrum; (b) high resolution Ag 3d spectrum and (c) high resolution O 1s spectrum.

Table 1 Measured XPS data from Ag 3d and O 1s spectra for electro-deposited Ag_xO nanostructures

	Ag $3d_{5/2}$		O 1s	
	BE/eV	at%	BE/eV	at%
As-deposited Ag_xO nanostructures	367.5	21	529.1	24
	368.1	79	531.3	68
			532.9	8
Ag_xO microparticles ⁵	367.9		529.5	
$\text{Ag}_2\text{O}^{6,30}$	367.9		529.4	
AgO^{31}	367.5		528.7	
			531.5	
AgO^{32}			529.0	
			530.7	

successfully. Therefore, each Ag 3d level can be deconvoluted into two splitting peaks, and the corresponding binding energies are tabulated in Table 1. The binding energies observed for the Ag_xO deposits are 367.5 eV and 368.1 eV, which are consistent with those of AgO and Ag_2O , respectively.^{5,30,31} The estimated percentages of the two splitting peaks (Ag^+ to Ag^{2+} ratio $\approx 80 : 20$) in Table 1 indicate that Ag^+ is the dominant silver oxidation state in the Ag_xO deposits.

Deconvolution of the O 1s spectrum gives valuable information regarding the chemical state of oxygen bonding in the Ag_xO deposits. A typical O 1s spectrum deconvoluted into its three components is shown in Fig. 4c with the results listed in Table 1. The broad peak with a binding energy of 532.9 eV can be generally assigned as the absorbed oxygenated species such as free water or carbon hydrated contaminations from atmosphere.^{6,7} The two peaks shown in the O 1s spectrum with binding energies of 529.1 and 531.3 eV are comparable to those observed in AgO samples in the literature.³² It is interesting to note that, in the AgO powder sample, the 529.0 eV peak is the predominant one⁶ while the major peak in the Ag_xO deposits is centered at 531.3 eV. This further confirms that the Ag_xO deposits are a mixture of Ag_2O and AgO with Ag^+ as dominant species.

3.3. Phase distribution and crystal structure

In order to understand the as-deposited Ag_xO nanostructures on finer scale, TEM and selected-area electron diffraction (SAED) were employed. Representative TEM micrographs and corresponding SAED ring patterns for the Ag_xO columnar structures prepared from the 0.001 M Ag(I) solution are shown in Fig. 5. Fig. 5a–c are taken from the Ag_xO columnar structure prepared at pH = 7.8 and 5 mA cm^{-2} . Fig. 5a confirms that the Ag_xO columnar structures are composed of stacked oxide nanoparticles with diameters ranging from 10 nm to 30 nm. The oxide particles are apparently embedded in a matrix of amorphous-like phase, rather than separated by grain boundaries. Careful examination of d -spacings of the SAED pattern in Fig. 5b indicates that this Ag_xO deposit has a cubic Ag_2O structure (space group $Pn\bar{3}$, JCPDS 76-1393),³³ but smaller d -spacing values can be observed when compared with the standard Ag_2O phase, as tabulated in Table 2. In a close-up high resolution TEM (HRTEM) image (Fig. 5c), it is apparent that amorphous zones exist between discrete crystalline oxide particles (areas defined by a white dashed curve in Fig. 5c), suggesting that each Ag_xO

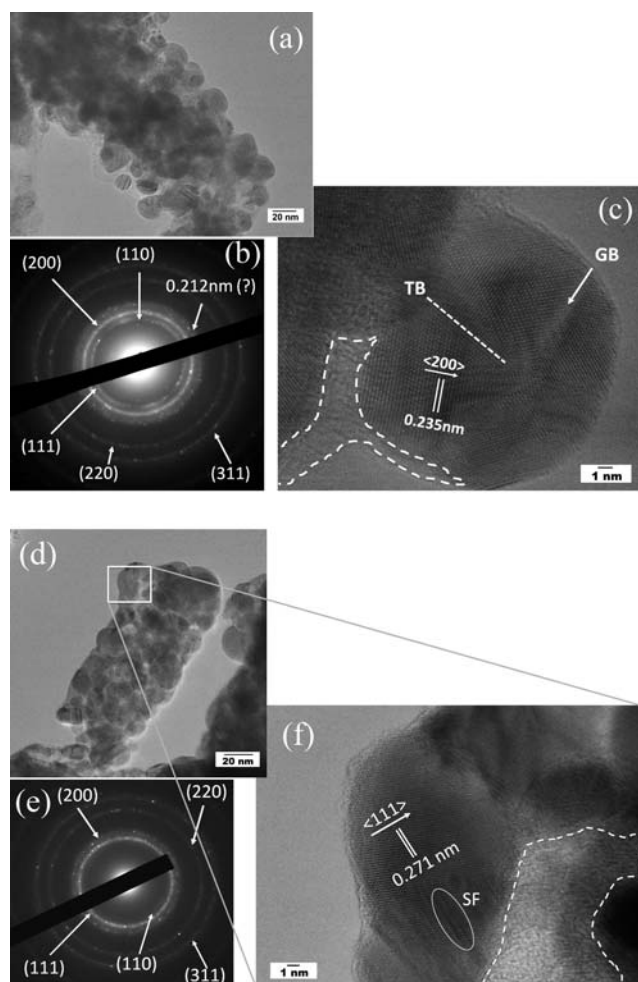


Fig. 5 TEM micrographs and SAED patterns taken from Ag_xO columnar structures: (a–c) 0.001 M $\text{Ag}(\text{I})$ solution, $\text{pH} = 7.8$ and 5 mA cm^{-2} ; (d–f) 0.001 M $\text{Ag}(\text{I})$ solution, $\text{pH} = 4.0$ and 5 mA cm^{-2} . GB, TB and SF denote grain boundary, twin boundary and stacking faults, respectively.

column is actually a composite of crystalline silver oxide particles plus an amorphous-like silver oxide phase. The HRTEM image also reveals that the Ag_xO particles are not fully crystalline. Crystallographic imperfections such as grain and twin boundaries can be seen within a single particle, shown as a straight dotted line and a white arrow in Fig. 5c.

Fig. 5d–f are the TEM micrographs and SAED pattern taken from the Ag_xO columns prepared from a 0.001 M $\text{Ag}(\text{I})$ solution at $\text{pH} = 4.0$ and 5 mA cm^{-2} . Similar physical features can be observed: nanoparticles with diameter on the order of tens of nanometres comprise the Ag_xO columns (Fig. 5d); the same cubic structure is assigned to the Ag_xO columns (Fig. 5e and Table 2); defects such as amorphous zones and stacking faults within the oxide particles are visible in the HRTEM image (Fig. 5f). As for the nanofibers and nanodisks prepared from a concentrated solution of 0.05 M $\text{Ag}(\text{I})$ (Fig. 3c and d), the corresponding TEM micrographs and SAED patterns are shown in Fig. 6. It is found that the nanofibers are polycrystalline in nature and composed of oxide particles (Fig. 6a), while each nanodisk is actually a single crystal with the cubic Ag_2O structure, which is confirmed by the spot SAED pattern in Fig. 6b.

The cubic Ag_2O structure can be described as a face-centered cubic (FCC) array of silver cations with oxygen anions occupying two of the eight tetrahedral interstices in the unit cell. The oxygen anion to metal cation ratio should be 1 : 2 in each unit cell. Based on the XPS analysis, the Ag^+ to Ag^{2+} ratio was estimated to be $\sim 4 : 1$, so the oxygen anion to silver cation ratio in the Ag_xO nanostructures is 1 : 1.67, which is significantly higher than what would be expected for a pure Ag_2O structure. This result suggests that the corner and face-centered positions in the FCC array are not fully occupied by silver cations (Ag deficiency is $1/6$ in a cubic Ag_2O unit cell), *i.e.*, anodic electrodeposition of Ag_xO tends to form a defective structure. A similar tendency has been observed in previous studies on anodic electrodeposition of metal oxides in the Mn-Co-O system.³⁴ From Table 2, it is apparent that the lattice parameters for the Ag_xO nanostructures (0.468–0.470 nm) are smaller than those for standard Ag_2O (0.476 nm). This difference in unit cell size can be attributed to the shorter cation–anion bond length for as-deposited silver oxides with a significant number of cation vacancies. In addition to the normal cubic Ag_2O diffraction rings, there is a diffraction ring between (200) and (220) reflections (Fig. 5b and 6a). The d -spacings for the extra diffraction rings are not consistent with any reflections for existing stable silver oxide phases, which may be attributed to partial ordering of Ag cation vacancies.

3.4. Growth mechanism

In the anodic electrodeposition of the Ag_xO deposits from AgNO_3 –sodium acetate solutions, $\text{Ag}(\text{I})$ cations are oxidized into AgO through the following anodic process:¹⁰

Table 2 Electron diffraction information for electrodeposited Ag_xO nanostructures

<i>d</i> -Spacing (nm)/Miller indices (<i>hkl</i>)			
Standard Ag_2O (JCPDS 76-1393)	Ag_xO columns-1 (Fig. 1b)	Ag_xO columns-2 (Fig. 2b)	Ag_xO nanofibers (Fig. 3b)
0.33658/(110)	0.331/(110)	0.330/(111)	0.332/(110)
0.27482/(111)	0.273/(111)	0.271/(111)	0.272/(111)
0.23800/(200)	0.236/(200)	0.235/(200)	0.236/(200)
0.19433/(211)	0.212(?)	—	0.210(?)
0.16829/(220)	0.165/(220)	0.163/(220)	0.192/(211)
0.14352/(311)	0.142/(311)	0.143/(311)	0.164/(220)
0.13741/(222)	0.134/(222)	0.134/(222)	0.144/(311)
			0.137/(222)
$a = 0.47600 \text{ nm}$	$a = 0.469 \text{ nm}$	$a = 0.468 \text{ nm}$	$a = 0.470 \text{ nm}$

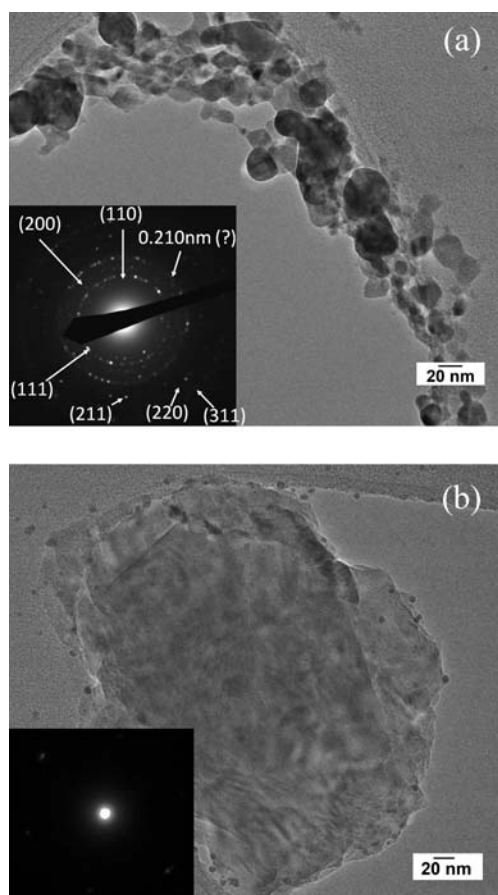


Fig. 6 TEM micrographs and SAED patterns taken from Ag_xO nanostructures. (a) 0.05 M $\text{Ag}(\text{I})$ solution, $\text{pH} = 7.0$ and 1 mA cm^{-2} ; (b) 0.05 M $\text{Ag}(\text{I})$ solution, $\text{pH} = 7.0$ and 0.1 mA cm^{-2} .



From the Pourbaix diagram for $\text{Ag}(\text{I})$ acetate solutions with various AgNO_3 concentrations calculated with HSC chemistry 6.0 software (Fig. 7), it is apparent that a reduction in $\text{Ag}(\text{I})$ concentration from 0.05 M to 0.001 M has slight influence on the electrooxidation potential of the $\text{Ag}(\text{I})$ cations, which is consistent with the Nernst equation. Moreover, with the reduction in $\text{Ag}(\text{I})$ concentration, the stable zone of $\text{Ag}(\text{I})$ is enlarged to a higher pH condition. Therefore, the kinetics of the electrodeposition process plays a more important role in the controlled growth of Ag_xO nanostructures. An essential issue in preparing oriented Ag_xO nanostructures is control of the nucleation and growth kinetics during electrodeposition, which is primarily determined by the supersaturation ratio of the condensing Ag_xO at the electrode/electrolyte interfaces.^{5,35} The supersaturation ratio can be adjusted by changing the electrodeposition parameters such as solution concentration, overpotential (current density) and solution pH.

Considering that the oxygen evolution potential is generally lower than the electrooxidation potential of the $\text{Ag}(\text{I})$ cations (Fig. 7), oxygen evolution occurs preferentially in a thermodynamic perspective and competes with Ag_xO formation during electrochemical deposition:

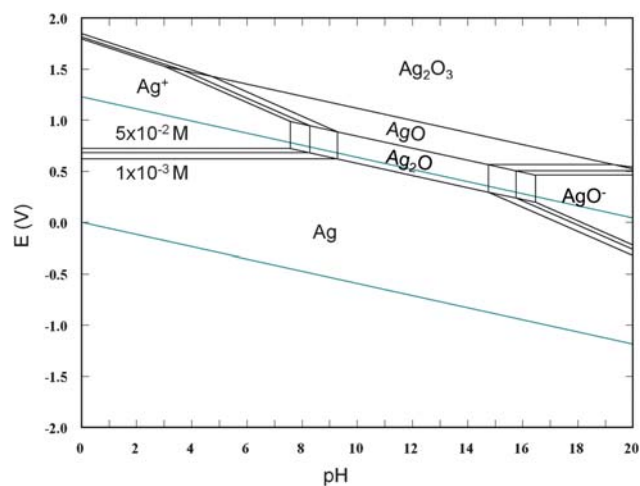
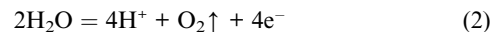


Fig. 7 Calculated $\text{Ag-H}_2\text{O}$ Pourbaix diagram for $\text{Ag}(\text{I})$ concentrations ranging from 0.05 M to 0.001 M.



Electrochemical analysis in a previous study confirmed that gas evolution becomes evident as the applied current density was increased to 1.0 mA cm^{-2} during electrodeposition.¹⁰ Oxygen evolution is an important process to account for the applied current density; the generated protons (eqn (2)) tend to consume the Ag_xO nuclei formed through eqn (1). In order to form Ag_xO deposits, a high supersaturation ratio of the condensing Ag_xO is required to compensate for the dissolved Ag_xO nuclei associated with the oxygen evolution process. A high supersaturation ratio generally leads to isotropic growth of Ag_xO nanoparticles, which may explain the polycrystalline nature of the Ag_xO columnar structures, as shown in Fig. 1, 2 and 5. The correlation between deposition parameters (supersaturation ratio) and physical features of Ag_xO nanostructures is illustrated as follows.

At a dilute concentration of 0.001 M $\text{Ag}(\text{I})$ and a low current density of 1 mA cm^{-2} , a low effective nucleation rate occurs during the initial stage of electrodeposition. This leads to the sparse Ag_xO deposits observed in Fig. 1a. Higher current densities of 5 and 20 mA cm^{-2} will generate more oxide nuclei on the electrode surfaces. Subsequent nucleation and growth of Ag_xO will occur preferentially on the small radii nanoparticles,³⁶ and to form columnar nanostructures with higher areal densities, shown in Fig. 1b and c. When the current densities are further increased to 50 mA cm^{-2} , a dilute $\text{Ag}(\text{I})$ concentration cannot supply enough $\text{Ag}(\text{I})$ species for Ag_xO formation. Protons generated by the predominant oxygen evolution process will consume a significant amount of the Ag_xO nuclei, leading to coarser columnar structures with increasing inter-column spacing (lower areal density) (Fig. 1d).

The same principle is applicable to explain the effect of pH on the morphology evolution of Ag_xO nanostructures. With the same dilute $\text{Ag}(\text{I})$ concentration and current density applied, a low pH value of 2.0 is not favorable to Ag_xO formation: only some rectangular columns are visible on the Au-coated glass substrates (Fig. 2a). With the pH values increased to 4.0 and 6.0, electro-oxidation of $\text{Ag}(\text{I})$ becomes favorable, so nucleation is

favored and Ag_xO deposits with smaller average diameters can be observed (Fig. 2b and c). From Fig. 7, $\text{Ag}(\text{I})$ species became unstable at a higher pH value of 9.5, *i.e.*, less available $\text{Ag}(\text{I})$ species in the solution. This may account for more sparse distribution of deposited Ag_xO columns observed in Fig. 2d. Note that the preferred shape of deposited Ag_xO columns is rectangular even when polycrystalline in character. Apparently, the growth process of these Ag_xO columns is different from those proposed for Ag_2O , Cu_2O and PbS crystals.^{5,37–39} Thus far, however, justification for a clear formation mechanism has not been reached.

In a higher concentration of 0.05 M $\text{Ag}(\text{I})$, the supersaturation ratio of Ag_xO is high even at a low current density, so no oriented structures are seen, but rather, densely packed Ag_xO deposits are detectable at a current density of 5 mA cm^{-2} (Fig. 3a). Upon application of a lower current density of 1 mA cm^{-2} , polycrystalline nanofibers with high areal density can be deposited (Fig. 3b and 6a). Further reduction in applied current density down to 0.1 mA cm^{-2} results in a different morphology, *i.e.*, vertically grown nanodisks (Fig. 3c and d). The spot diffraction pattern taken from a single Ag_xO nanodisk confirms its single crystal nature. A low supersaturation ratio of Ag_xO species enables epitaxial growth, thus resulting in the formation of disk-shaped Ag_xO nanostructures.

The shape, diameter and areal density of the oriented Ag_xO nanostructures can be adjusted through the control of current density, concentration of silver nitrate and solution pH. Among these three deposition parameters, the concentration of silver nitrate exerts the most significant effect on the physical feature evolution of Ag_xO nanostructures. Discrete columnar structures tend to form in a dilute $\text{Ag}(\text{I})$ system, while a variety of nanostructures could be obtained from a concentrated $\text{Ag}(\text{I})$ system. Variation in current density and pH value will affect the diameter and areal density of the Ag_xO nanostructures. It is believed that the rich morphology of Ag_xO obtained in this work is primarily determined by the impact of supersaturation ratio on reaction kinetics in the aqueous solutions.

4. Conclusion

A facile, template-free electrochemical route has been developed to deposit Ag_xO nanostructures on conductive substrates from aqueous solutions. The physical features (shape, diameter and areal density) of the Ag_xO nanostructures were adjusted through control of the current density, concentration of silver nitrate and solution pH. In a dilute $\text{Ag}(\text{I})$ system, a polycrystalline columnar structure is preferred; the diameter and areal density of the Ag_xO columns are sensitive to the applied current density and solution pH. In a concentrated $\text{Ag}(\text{I})$ system, densely packed Ag_xO deposits evolve into high areal density polycrystalline nanofibers and single crystalline nanodisks, as the applied current density is decreased from 5 mA cm^{-2} to 0.1 mA cm^{-2} . Structural and chemical analyses, based on TEM/SAED and XPS, confirm that the Ag_xO nanostructures have a defective cubic Ag_2O structure. The variety of nanostructures obtained in this work can be ascribed to the kinetic aspect of supersaturation ratio in the aqueous solutions.

Acknowledgements

The authors acknowledge financial support from Z-Power Inc. This work made use of the MRSEC Shared Experimental Facilities at MIT, supported by the National Science Foundation under award number DMR-08-19762.

References

- 1 J. F. Pierson and C. Rousselot, *Surf. Coat. Technol.*, 2005, **200**, 276.
- 2 J. F. Weaver and G. B. Hoflund, *J. Phys. Chem.*, 1994, **98**, 8519.
- 3 M. Biemann, P. Schwaller, P. Ruffieux, O. Groning, L. Schlapbach and P. Groning, *Phys. Rev. B: Condens. Matter Mater. Phys.*, 2002, **65**, 235431.
- 4 N. Yamamoto, S. Tonomura, T. Matsuoka and H. Tsubomura, *Jpn. J. Appl. Phys.*, 1981, **20**, 721.
- 5 B. J. Murray, Q. Li, J. T. Newberg, E. J. Menke, J. C. Hemminger and R. M. Penner, *Nano Lett.*, 2005, **5**, 2319.
- 6 B. J. Murray, Q. Li, J. T. Newberg, E. J. Menke, J. C. Hemminger and R. M. Penner, *Chem. Mater.*, 2005, **17**, 6611.
- 7 B. J. Murray, J. T. Newberg, E. C. Walter, Q. Li, J. C. Hemminger and R. M. Penner, *Anal. Chem.*, 2005, **77**, 5205.
- 8 E. Tselepis and E. Fortin, *J. Mater. Sci.*, 1986, **21**, 985.
- 9 Y. Ida, S. Watase, T. Shinagawa, M. Watanabe, M. Chigane, M. Inaba, A. Tasaka and M. Izaki, *Chem. Mater.*, 2008, **20**, 1254.
- 10 B. E. Breyfogle, C. Hung, M. G. Shumsky and J. A. Switzer, *J. Electrochem. Soc.*, 1996, **143**, 2741.
- 11 Y. Her, Y. Lan, W. Hsu and S. Y. Tsai, *J. Appl. Phys.*, 2004, **96**, 1283.
- 12 J. Tominaga, *J. Phys.: Condens. Matter*, 2003, **15**, R1101.
- 13 W. A. Parkhurst, S. Dallek and B. F. Larrick, *J. Electrochem. Soc.*, 1984, **131**, 1739.
- 14 S. Dallek, W. A. West and B. F. Larrick, *J. Electrochem. Soc.*, 1986, **133**, 2451.
- 15 D. Buchel, C. Mihalcea, T. Fukaya, N. Atoda, J. Tominaga, T. Kikuwa and H. Fuji, *Appl. Phys. Lett.*, 2001, **79**, 620.
- 16 S. Haratani, J. Tominaga, H. Dohi and S. Takayama, *J. Appl. Phys.*, 1994, **76**, 1297.
- 17 T. Fukaya, D. Buchel, S. Shinbori, J. Tominaga, N. Atoda, D. P. Tsai and W. Lin, *J. Appl. Phys.*, 2001, **89**, 6139.
- 18 S. S. Djokic, R. E. Burrell, N. Le and D. J. Field, *J. Electrochem. Soc.*, 2001, **148**, C191.
- 19 Y. Chiu, U. Rambabu, M. Hsu, H. Shieh, C. Y. Chin and H. H. Lin, *J. Appl. Phys.*, 2003, **94**, 1996.
- 20 T. Shima and J. Tominaga, *J. Vac. Sci. Technol., A*, 2003, **21**, 634.
- 21 Y. Abe, T. Hasegawa, M. Kawamura and K. Sasaki, *Vacuum*, 2004, **76**, 1.
- 22 A. V. Kolobov, A. Rogalev, F. Wilhelm, N. Jaouen, T. Shima and J. Tominaga, *Appl. Phys. Lett.*, 2004, **84**, 1641.
- 23 J. F. Pierson, D. Wiederkehr and A. Billard, *Thin Solid Films*, 2005, **478**, 196.
- 24 T. Arai, C. Rockstuhl, P. Fons, K. Kurihara, T. Nakano, K. Awazu and J. Tominaga, *Nanotechnology*, 2006, **17**, 79.
- 25 A. A. Schmidt, J. Offermann and R. Anton, *Thin Solid Films*, 1996, **281–282**, 105.
- 26 S. M. Hou, M. Ouyang, H. F. Chen, W. M. Liu, Z. Q. Xue, Q. D. Wu, H. X. Zhang, H. J. Gao and S. J. Pang, *Thin Solid Films*, 1998, **315**, 322.
- 27 K. Byrappa and T. Adschiri, *Prog. Cryst. Growth Charact. Mater.*, 2007, **53**, 117, and references therein.
- 28 X. M. Chen and M. L. Tong, *Acc. Chem. Res.*, 2007, **40**, 162, and references therein.
- 29 J. A. Switzer, in *Electrochemistry of Nanomaterials: Preparations and Properties*, ed. G. Hodes, Wiley-Vch, Weinheim, 2001, p. 67.
- 30 J. S. Hammond, S. W. Gaarenstroom and N. Winograd, *Anal. Chem.*, 1975, **47**, 2193.
- 31 J. Chastain, *Handbook of X-Ray Photoelectron Spectroscopy*, Perkin-Elmer Corp., Eden Prairie, MN, 1992.
- 32 M. Biemann, P. Schwaller, P. Ruffieux, O. Groning, L. Schlapbach and P. Groning, *Phys. Rev. B: Condens. Matter Mater. Phys.*, 2002, **65**, 235431.
- 33 JCPDS, International Center for Diffraction Data, Newtown Square, PA, 2001.

-
- 34 W. F. Wei, W. X. Chen and D. G. Ivey, *J. Phys. Chem. C*, 2007, **111**, 10398.
- 35 I. Sunagawa, *Crystals Growth, Morphology and Perfection*, Cambridge University Press, Cambridge, 2005.
- 36 S. C. Hill and J. I. D. Alexander, *Phys. Rev. E: Stat. Phys., Plasmas, Fluids, Relat. Interdiscip. Top.*, 1997, **56**, 4317.
- 37 D. B. Wang, M. S. Mo, D. B. Yu, L. Q. Xu, F. Q. Li and Y. T. Qian, *Cryst. Growth Des.*, 2003, **3**, 717.
- 38 Y. H. Ni, H. J. Liu, F. Wang, Y. Y. Liang, J. M. Hong, X. Ma and Z. Xu, *Cryst. Growth Des.*, 2004, **4**, 759.
- 39 X. Wang, H. F. Wu, Q. Kuang, R. B. Huang, Z. X. Xie and L. S. Zheng, *Langmuir*, 2010, **26**, 2774.